Direct parametric reconstruction from undersampled (**k**, t)-space data in dynamic contrast enhanced MRI

Nikolaos Dikaios [a,b,*], Simon Arridge [b], Valentin Hamy [a], Shonit Punwani [a], David Atkinson [a]

[a] Centre for Medical Imaging, University College London, 250 Euston Road, NW1 2PG London, UK
[b] Centre for Medical Image Computing, University College London, Gower Street, WC1E 6BT London, UK

ABSTRACT

The Magnetic Resonance Imaging (MRI) signal can be made sensitive to functional parameters that provide information about tissues. In dynamic contrast enhanced (DCE) MRI these functional parameters are related to the microvasculature environment and the concentration changes that occur rapidly after the injection of a contrast agent. Typically DCE images are reconstructed individually and kinetic parameters are estimated by fitting a pharmacokinetic model to the time-enhancement response; these methods can be denoted as "indirect". If undersampling is present to accelerate the acquisition, techniques such as kt-FOCUSS can be employed in the reconstruction step to avoid image degradation. This paper suggests a Bayesian inference framework to estimate functional parameters directly from the measurements at high temporal resolution. The current implementation estimates pharmacokinetic parameters (related to the extended Tofts model) from undersampled (**k**, t)-space DCE MRI. The proposed scheme is evaluated on a simulated abdominal DCE phantom and prostate DCE data, for fully sampled, 4 and 8-fold undersampled (**k**, t)-space data. Direct kinetic parameters demonstrate better correspondence (up to 70% higher mutual information) to the ground truth kinetic parameters (of the simulated abdominal DCE phantom) than the ones derived from the indirect methods. For the prostate DCE data, direct kinetic parameters depict the morphology of the tumour better. To examine the impact on cancer diagnosis, a peripheral zone prostate cancer diagnostic model was employed to calculate a probability map for each method.

1. Introduction

Dynamic contrast enhanced-magnetic resonance imaging (DCE-MRI) is a common imaging biomarker of vasculature and perfusion. DCE-MRI is mainly used for the diagnosis of cancer in different anatomical regions such as the prostate (Buckley et al., 2004), the head and neck (Agrawal et al., 2012), the breast (Furman-Haran et al., 2013), the cervix (Andersen et al., 2013), the brain (Jain, 2013) and the liver (Armbruster et al., 2014).

Briefly, in DCE-MRI a paramagnetic contrast agent (Gadolinium) is administered via intravenous injection, resulting in shortening of the $T1$ relaxation time from its native value $T10$.

$$\frac{1}{T1(\mathbf{r}, t; w)} = \frac{1}{T10(\mathbf{r})} + r_1 \cdot C(\mathbf{r}, t \geqslant t_0; w) \tag{1}$$

$C(\mathbf{r}, t; w) \in \mathbf{C}^{M \times J}$ is the concentration of the contrast agent, $\mathbf{r}$ is the spatial coordinate, M is the number of spatial pixels and J is the number of dynamic acquisitions, $w(\mathbf{r})$ are parameters related to the contrast agent kinetics and dictate the enhancement, r_1 is the relaxivity and t_0 is the arrival time of the bolus at the tissue. The concentration of the contrast agent in the extracellular extravascular space (EES) can be described by the extended Tofts model (Tofts, 1997) using the tracer kinetic parameters $w(\mathbf{r}) = \{v_p(\mathbf{r}), K_{\text{trans}}(\mathbf{r}), v_e(\mathbf{r}), t_0(\mathbf{r})\}$.

$$C(\mathbf{r}, t; w) = v_p(\mathbf{r}) \cdot C_p(\mathbf{r}, t) + K_{\text{trans}}(\mathbf{r}) \cdot \int_0^t C_p(\mathbf{r}, \tau - t_0)$$
$$\otimes e^{\left(-\frac{K_{\text{trans}}(\mathbf{r})}{v_e(\mathbf{r})}(t - \tau) \right)} d\tau \tag{2}$$

C_p (mmol/L) is the arterial input function (AIF), v_p is the blood plasma volume, K_{trans} (min^{-1}) is the volume transfer constant between plasma and the EES, and v_e is the EES volume. If a population average AIF (Parker et al., 2006) is used, the arrival time of the bolus to the tissue is unknown hence the onset time t_0 will need to be taken into account.

DCE-MRI employs fast $T1$ weighted sequences for which the received signal can be modelled by

* Corresponding author at: Centre for Medical Imaging, University College London, 250 Euston Road, NW1 2PG London, UK. Tel.: +44 75575 38412.
  E-mail address: n.dikaios@ucl.ac.uk (N. Dikaios).

$$S(\boldsymbol{k}, t; w) = \int x(\boldsymbol{r}, t; w) \cdot \exp(-j2\pi \boldsymbol{k} \cdot \boldsymbol{r}) d\boldsymbol{r}$$

$$= \int S_0(\boldsymbol{r}) \frac{\sin(\alpha) \cdot \left(1 - \exp\left(-\frac{TR}{T1(\boldsymbol{r}, t; w)}\right)\right)}{1 - \cos(\alpha) \cdot \exp\left(-\frac{TR}{T1(\boldsymbol{r}, t; w)}\right)} \cdot \exp(-j2\pi \boldsymbol{k} \cdot \boldsymbol{r}) d\boldsymbol{r} \quad (3)$$

$S(\mathbf{k}, t) \in \mathbf{C}^{K \times J}$, is in the spatial frequency domain, K is the number of spatial frequency samples, the modelled enhancement signal is $x(\mathbf{r}, t; w)$, $S_0(\mathbf{r})$ is the proton density image, TR is the repetition time and α is the flip angle.

Some of the important microvascular exchanges occur rapidly hence high temporal resolution is necessary to capture the enhancement process especially immediately after the contrast agent is injected. The temporal resolution of the acquisition can be improved using undersampling techniques in $(\mathbf{k}, t)$-space.

Parallel imaging techniques can increase the temporal resolution by reducing the number of phase encoding steps and using knowledge of coil sensitivities in the reconstruction (Pruessmann et al., 1999; Griswold et al., 2002).

Compressed sensing (CS) is an emerging theory from signal processing (Donoho, 2006) that can recover images using a non-linear reconstruction from undersampled data by promoting sparsity in an image transform domain. In MRI, the artifacts due to undersampling of the k-space data must be incoherent in the image transform domain. Several CS techniques have been proposed for reconstruction of dynamic MR data, a popular scheme is kt-SPARSE (Lustig et al., 2007), which minimizes an l_1-norm objective function

$$min_z \|\Phi z\|_1 \, s.t. \|F_u z - y_2\| < \varepsilon \quad (4)$$

where $\|\cdot\|_1$ is the l_1-norm, F_u is a Fourier sampling operator, y is the acquired signal, Φ is an operator that in DCE MRI reconstruction would transform the modelled signal $z(\mathbf{r}, t)$ to a sparse representation (i.e. a wavelet transform in the spatial direction and a Fourier transformation in the temporal direction) and ε is a small number usually set at the noise level. Another popular sparse reconstruction algorithm is focal underdetermined system solver (kt-FOCUSS) based on work of Gorodnitsky et al. (1995) and modified by Jung et al. (2007) to become suitable for dynamic MRI applications. A more detailed description of the kt-FOCUSS algorithm follows in the theory section. Dynamic reconstruction can also involve low rank matrix completion techniques which are usually combined with sparsity (Gao et al., 2011; Lingala et al., 2011). A popular rank minimization technique is the kt-SLR algorithm proposed by (Lingala et al., 2011) which minimizes a cost function that involves a rank prior $\Psi_1(z)$, and a sparsity prior $\Psi_2(z)$.

$$min_z \|F_u z - y\|_2^2 + \lambda_1 \Psi_1(z) + \lambda_2 \Psi_2(z) \quad (5)$$

For more information about temporal acceleration MR reconstruction techniques readers can refer to a review by Tsao and Kozerke (2012).

Traditional DCE analysis fits the pharmacokinetic parameters $w(\mathbf{r})$ related to the extended Tofts model so that the modelled enhancement signal $x(\mathbf{r}, t; w)$ is close to the reconstructed dynamic MR data $z(\mathbf{r}, t)$.

In this work we suggest a direct estimation of the kinetic parameters from undersampled dynamic $(\mathbf{k}, t)$-space data with a Bayesian inference algorithm. An overview of the algorithm is shown in Fig. 1.

The suggested scheme is evaluated on a simulated DCE MRI abdominal phantom, and on simulated prostate DCE MRI measurements for undersampling acceleration factors of 4 and 8. The performance of the suggested scheme is compared against indirect approaches where dynamic contrast enhanced MR data were reconstructed using zero-filled fast Fourier transformation or

kt-FOCUSS and kinetic parameters $w(\mathbf{r})$ were fit to these reconstructed images using the extended Tofts model.

2. Theory

2.1. Focal underdetermined system solver (kt-FOCUSS)

kt-FOCUSS is computationally efficient and was shown to recover accurate solutions even for highly undersampled $(\mathbf{k}, t)$-space data. kt-FOCUSS uses a "soft " sparse constraint suitable for dynamic MR reconstruction, and is implemented as a re-weighted quadratic optimization (Jung et al., 2007). kt-FOCUSS minimizes an unconstrained cost function, which aims to recover the space by frequency r–f image $\rho = Hq$

$$min_q \|FHq - y\|_2^2 + \lambda \|q\|_2^2 \quad (6)$$

where λ is the Lagrangian multiplier, F is the 2D Fourier transform along the r–f direction, H is a weighting matrix and q is the solution of the minimization. In other words, q is minimizing the quadratic optimization and H is re-weighting q. The r–f image ρ is initialized from interleaved low-frequency $(\mathbf{k}, t)$-data. The resulting low resolution image is used to initialize the weighting matrix H and this solution is pruned to achieve a sparser image. The image is transformed to the r–f space because it is sparser in that domain, especially if the signal follows a periodic motion. This process is repeated iteratively (Jung et al., 2007).

2.2. Hierarchical Bayesian inference algorithm

2.2.1. Hierarchical Bayesian inference algorithm

The acquired T1 weighted signal $y(\mathbf{k}, t) \in \mathbf{C}^{K \times J}$, is in the spatial frequency domain, where K is the number of spatial frequency samples per dynamic, and J is the number of dynamic acquisitions. The acquired signal can be modelled, $S(\mathbf{k}, t; w)$ as shown in (3) based on the pharmacokinetic parameters, $w(\mathbf{r}) = \{v_p(\mathbf{r}), K_{\text{trans}}(\mathbf{r}), v_e(\mathbf{r}), t_0(\mathbf{r})\}$ of the extended Tofts model assuming Gaussian noise σ on the acquired signal.

$$y(\mathbf{k}, t) \sim \mathbf{normal}(S(\mathbf{k}, t; w), \sigma) \quad (7)$$

The suggested Bayesian inference algorithm maximizes the posterior probability distribution function $p(x(w), \sigma|y)$ as a function of $w(\mathbf{r})$ and σ

$$\hat{w}, \hat{\sigma} = argmax_{w,\sigma} p(x(w), \sigma|y) \quad (8)$$

According to the Bayes theorem $p(x(w), \sigma|y)$ is given by,

$$p(x(w), \sigma|y) = \frac{p(x(w), \sigma) \cdot p(y|w, \sigma)}{\int_{w^*, \sigma^*} p(x(w^*), \sigma^*) \cdot p(y|w^*, \sigma^*)} \quad (9)$$

where

- $p(y|w, \sigma)$ is the likelihood function of $y(\mathbf{k}, t)$ given the model parameters w,

$$p(y|w, \sigma) = (2\pi\sigma^2)^{-K \cdot J} \exp\left(-\frac{1}{2\sigma^2} \|y(\boldsymbol{k}, t) - S(\boldsymbol{k}, t; w)\|_2^2\right) \quad (10)$$

- $p(x(w), \sigma)$ is the product of the prior probability distribution functions of $x(\mathbf{r}, t; w)$ and σ, i.e. $p(x(w), \sigma) = p(x(w)) \times p(\sigma)$.

Prior probability distribution functions $p(x; w)$, $p(\sigma)$ reflect our prior knowledge about the $x(\mathbf{r}, t; w)$ and σ parameters.

- a low rank prior on the dynamic enhancement signal $x(\mathbf{r}, t; w) \in \mathbf{R}^{M \times J}$ in the image domain to promote local coherence in time,

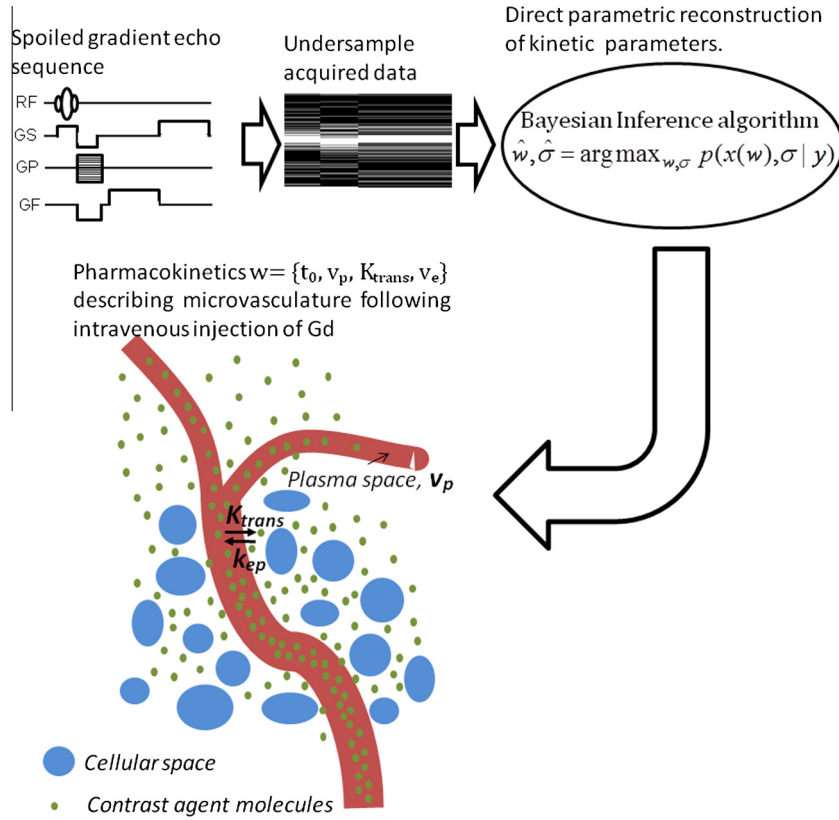$$p(x; w) = (\exp(-\lambda \cdot \|x(r, t; w)\|_*),$$

Fig. 1. Diagram illustrating the dependence of the acquired signal on the microvasculature processes as described by the extended Tofts model: Blood plasma volume v_p, volume transfer constant between plasma and EES (min^{-1}) K_{trans}, EES volume v_e. Following the acquisition of undersampled dynamic ($\boldsymbol{k}$–t)-data, direct parametric reconstruction aims to recover the kinetic parameters associated with the extended Tofts model.

$\|\cdot\|_*$ is the nuclear norm and $\lambda \in \mathbf{R}^+$ is a regularization parameter. The nuclear norm of a matrix is the sum of its singular values, $\| \cdot \|_* = \|sing(\cdot)\|_1$. The nuclear norm is the largest convex function bounded by the rank function.

- Gaussian prior for the kinetic parameters $w(\mathbf{r})$. We assume that they remain positive and within a certain range,
- an uninformative Inverse Gamma (IG) prior is used for the unknown variance σ^2 of the noise,

$$p(\sigma^2) = IG(\sigma^2|a,b) = (b^a/\Gamma(a)) \cdot \sigma^{-2(a-1)} \cdot \exp(-b\sigma^{-2}),$$

a, b are the scale and shape parameter respectively. We set a, $b = 10^{-4}$. For the limit $a, b \to 0$ it yields an improper posterior density. For low σ values inferences will become very sensitive to a, b and the IG is no longer non-informative any more.

The use of additional sparsity priors in the dynamic enhancement signal (l_1 norm of the wavelet or total variation transform) was examined but did not benefit the algorithm.

The maximization of the aforementioned posterior probability distribution function $p(w, \sigma|y)$, would be similar to the problem of minimizing the unconstrained Lagrangian version of the nuclear norm relaxation from undersampled measurements $y(\mathbf{k}, t)$,

$$\hat{w} = argmin_w h(w)$$

$$= argmin_w \frac{1}{2} \|y(\boldsymbol{k},t) - F_u x(r,t;w)\|_2^2 + \lambda \cdot \|x(\boldsymbol{r},t;w)\|_* \quad (11)$$

where $F_u \in \mathbf{R}^{M\times J} \to \mathbf{C}^{T\times J}$ is a Fourier sampling operator, with $T \leqslant K$. Cost function h is strictly convex hence its sub differential at w is

$$\partial h(w) = \{v : h(v) \geqslant h(w) + u^T(v-w), \forall v \in R^M\} \quad (12)$$

where u^T is a subgradient of h at w, $\hat{w}$ is the optimal minimizer $\hat{w} \in argmin_w h(w)$, iff $0 \in \partial h(\hat{w})$.

Theorem 2.1 by Cai et al. (2008) states that the singular shrinkage operator $D_\lambda(x(\boldsymbol{r},t;w))$ is the proximity operator of $\lambda \cdot \|x(\boldsymbol{r},t;w)\|_*$. The singular value shrinkage operator is defined as

$$D_\lambda(x) = U\mathcal{S}_\lambda(\Sigma)V^*$$
$$\mathcal{S}_\lambda(\Sigma) = sign(\Sigma) \cdot \max(|\Sigma| - \lambda, 0) \quad (13)$$

$\mathcal{S}_\lambda$ is the shrinkage operator, and $x = U\Sigma V^*$ is any singular value decomposition of x, where Σ is the rectangular diagonal matrix, and U, V are the left and right singular vectors.

Combettes and Wajs (2005) provided a solution to the unconstrained problem of Eq. (11). Cai et al. (2008) described a simplified version of the iterative soft thresholding algorithm (Eq. (2.10)), which in our case can be expressed as

$$x(r,t;w^k) = D_\lambda(x(r,t;w^k)) \quad (14)$$

$$w^{k+1} = w^k - \lambda \cdot (\nabla_w x(r,t;w^k)) \cdot F_u^T(y(\boldsymbol{k},t) - F_u x(r,t;w^k)) \quad (15)$$

Updates for each w parameter from the minimization of (11) are employed in the Bayesian scheme and as aforementioned we assume they follow Gaussian distribution.

$$\hat{w} = \textbf{normal}(w, \sigma_w) \quad (16)$$

where σ_w is the standard deviation for each of the modelled parameters $v_p(\mathbf{r})$, $K_{trans}(\mathbf{r})$, $v_e(\mathbf{r})$, $t_0(\mathbf{r})$.

The integral $\int_{w^*, \sigma^*} p(w^*, \sigma^*)$ cannot be calculated analytically, consequently $p(x(w), \sigma|y)$ is estimated with the Metropolis–Hastings algorithm, which is a Markov chain Monte Carlo method.

From the most recent sample parameters, candidate sample parameters are generated using a proposal density that must be symmetric, and probability space is explored using a random walk. The proposed density was a normal distribution.

2.2.2. Implementation of Bayesian inference algorithm

We first initialize the pharmacokinetic parameters $w(\mathbf{r}) = \{v_p(\mathbf{r}), K_{\text{trans}}(\mathbf{r}), v_e(\mathbf{r}), t_0(\mathbf{r})\}$, the noise σ of the acquired signal, and the noise of the model parameters, σ_{vp}, σ_{Ktrans}, σ_{ve}, σ_{t0} respectively as follows.

For iteration $i = 0$ and $\forall \mathbf{r} \in \mathbf{R}^{M \times J}$

   i. $v_p^{(0)}(\mathbf{r}) = 0.05$, $\sigma_{\text{vp}}^{(0)}(\mathbf{r}) = 0.1$.

   ii. $K_{\text{trans}}^{(0)}(\mathbf{r}) = 0.5$, $\sigma_{\text{Ktrans}}^{(0)}(\mathbf{r}) = 0.1$.

   iii. $v_e^{(0)}(\mathbf{r}) = 0.7$, $\sigma_{\text{ve}}^{(0)}(\mathbf{r}) = 0.1$.

   iv. $t_0^{(0)}(\mathbf{r})$, $\sigma_{\text{t0}}^{(0)}(\mathbf{r})$ will depend on the bolus injection time.

   v. $\sigma^2 = \text{IG}(a = 10^{-4}, b = 10^{-4})$.

The aforementioned initializations have been used throughout the paper.

The nuclear norm minimization described in Eq. (3) is employed to generate the recent $x(\mathbf{r}, t; w^{(i)})$, recent model parameters $w^{(i)}$ are estimated separately using Eqs. (14) and (15). The enhancement signal is formulated as a Casorati matrix, which is likely to be low rank because there is an expected correlation between images (columns of the Casorati matrix). This prior is incorporated to ensure that the algorithm can handle undersampled data. If the algorithm was solely a nuclear norm minimization, then the noise of the acquired data would not be modelled and it could not benefit from the convergence properties of the Bayesian inference algorithm used here (Gelman and Shirley, 2011). From each of the model parameters $w^{(i)}$, separate candidate sample parameters $w^{(i+1)}$ were generated using a proposal density $Q(w^{(i+1)}|w^{(i)})$. $Q(w^{(i+1)}|w^{(i)})$ must be symmetric and explore probability space using a random walk. Although the selection of proposal density is not trivial and can affect convergence (Rosenthal, 2010), normal proposal distributions usually work well in practice and this is why they were chosen in this scheme.

   i. $v_p^{(i+1)}(\mathbf{r}) \sim \text{\textbf{normal}}(v_p^{(i)}(\mathbf{r}), \sigma_{\text{vp}}^{(i)}(\mathbf{r}))$.

   ii. $K_{\text{trans}}^{(i+1)}(\mathbf{r}) \sim \text{\textbf{normal}}(K_{\text{trans}}^{(i)}(\mathbf{r}), \sigma_{\text{Ktrans}}^{(i)}(\mathbf{r}))$.

   iii. $v_e^{(i+1)}(\mathbf{r}) \sim \text{\textbf{normal}}(v_e^{(i)}(\mathbf{r}), \sigma_{\text{ve}}^{(i)}(\mathbf{r}))$.

   iv. $t_0^{(i+1)}(\mathbf{r}) \sim \text{\textbf{normal}}(t_0^{(i)}(\mathbf{r}), \sigma_{\text{t0}}^{(i)}(\mathbf{r}))$.

Acceptance thresholds are calculated for each sample parameter separately, and candidate sample parameters are rejected or accepted

  threshold = $p(w^{(i+1)}, \sigma^{(i)}|y) / p(w^{(i)}, \sigma^{(i)}|y)$

    If threshold $\leqslant$ rand then $w^{(i+1)} = w^{(i)}$ (i.e. reject candidate)

    else if threshold $\geqslant$ rand then accept candidate

where rand is a pseudorandom number generated from standard uniform distribution on the open interval (0, 1).

Sample $\sigma^{(i+1)}$ is updated using the probability density function $p(\sigma|w^{(i+1)}, y) \sim p(\sigma) \times p(y|w^{(i+1)}, \sigma)$,

$$p(\sigma|w^{(i+1)}, y) \sim \sigma^{-2(a-1)} \cdot \sigma^{-kJ} \cdot \exp\left(-\frac{1}{2\sigma^2}\|y(\mathbf{k}, t) - S(\mathbf{k}, t)\|_2^2\right) \tag{17}$$

This is a form of a gamma distribution, $G(a^*, b^*)$ with

$$a^* = a + \frac{K \cdot J}{2} \quad \text{and} \quad b^* = b + \frac{1}{2}\|y(\mathbf{k}, t) - S(\mathbf{k}, t)\|_2^2 \tag{18}$$

The prior probability distribution $p(w)$ depends on hyper-parameters $\{\sigma_{\text{vp}}, \sigma_{\text{Ktrans}}, \sigma_{\text{ve}}, \sigma_{\text{t0}}\}$ that are tuned automatically. For each hyper-parameter an acceptance probability is defined as the percentage of the times the respective candidate sample parameters (one of $v_p(\mathbf{r})$, $K_{\text{trans}}(\mathbf{r})$, $v_e(\mathbf{r})$, $t_0(\mathbf{r})$) has been accepted.

If the acceptance probability falls within a certain range [0.3, 0.6] the hyper-parameters are kept the same, otherwise they are modified (scaled).

It is assumed that Markov chain reaches the target distribution after a number of iterations (denoted as burn-in iteration); hence the variables from the early iterations are thrown away. To reduce sample correlations, thinning was used and only every thin[th] draw (thinning iteration) from the Markov chain was kept. If for example the thinning variable is equal to 5, only the samples from the mod(i, 5) equal to zero iteration will be kept.

3. Materials and methods

3.1. Optimization details

The techniques described were implemented in MATLAB (The Mathworks Inc., Natick, MA).

The proposed Bayesian inference algorithm was implemented as a Metropolis–Hastings algorithm. Section 2.2.2 describes how the involved parameters were initialized. The total number of iterations was 500, burn-in iterations were 300, thinning equal to 5, and tune iteration (number of iterations for tuning) was 67.

This approach was compared against techniques that fit the modelled enhancement signal to the reconstructed dynamic enhancement images and are denoted as "indirect". For the indirect techniques, DCE images were reconstructed with either fast Fourier transformation after zero-filling (denoted as "Indirect (ZF-FFT)"), or kt-FOCUSS (denoted as "Indirect(ktFOCUSS)"). The parameter settings for kt-FOCUSS (Jung et al., 2007) were 40 inner iterations, 2 outer iterations, weighting matrix power factor 0.5, and initial estimate corresponding to low-frequency values.

The fitting algorithm minimizes the l_1-norm (Press et al., 1984) between the reconstructed measured data and the modelled enhancement signal with a simplex algorithm (fminsearch in MATLAB). To avoid local minima, the onset time t_0 was randomly initialized 20 times and the pharmacokinetic parameters that best fit the data were reported.

3.2. Generation of simulated abdominal DCE ($\mathbf{k}$, t)-data

A normal volunteer underwent a fast gradient echo DCE-MRI protocol (flip angle 10°, repetition time 2.3 ms). Informed consent and ethical approval was obtained.

$T1$-weighted abdominal images were acquired in multiple time frames without contrast injection. The first time-frame was manually segmented into: liver, bowel, right and left heart, aorta, portal vein. Such segmentation was used as a map to simulate contrast enhancement using the extended Tofts model and a population arterial input function (Parker et al., 2006). $T1$ values were taken from (Tofts, 2010) and pharmacokinetic parameters for each organ were chosen in agreement with a previous study (Melbourne et al., 2008). Fifty DCE images were generated from the ground truth kinetic parameters with temporal resolution 3 s; and were transformed to ($\mathbf{k}$, t)-space with fast Fourier transformation. The noise of complex valued ($\mathbf{k}$, t)-space MR data can be reasonably modelled by an additive white Gaussian distribution on both real and imaginary components (with i.i.d. random variables) (Gudbjartsson and Patz, 2005). The level of noise was adjusted to achieve a signal to noise ratio (SNR) similar to the one reported in liver studies in the literature (Banerji et al., 2012). In practice the SNR is not known and here the SNR of the abdominal images was determined using a noise estimation algorithm (Coupe et al., 2010; Dikaios et al., 2013a). One of the advantages of modelling noise in the acquired ($\mathbf{k}$, t)-space domain is that it does not suffer from spatial variations that are caused by image reconstruction.
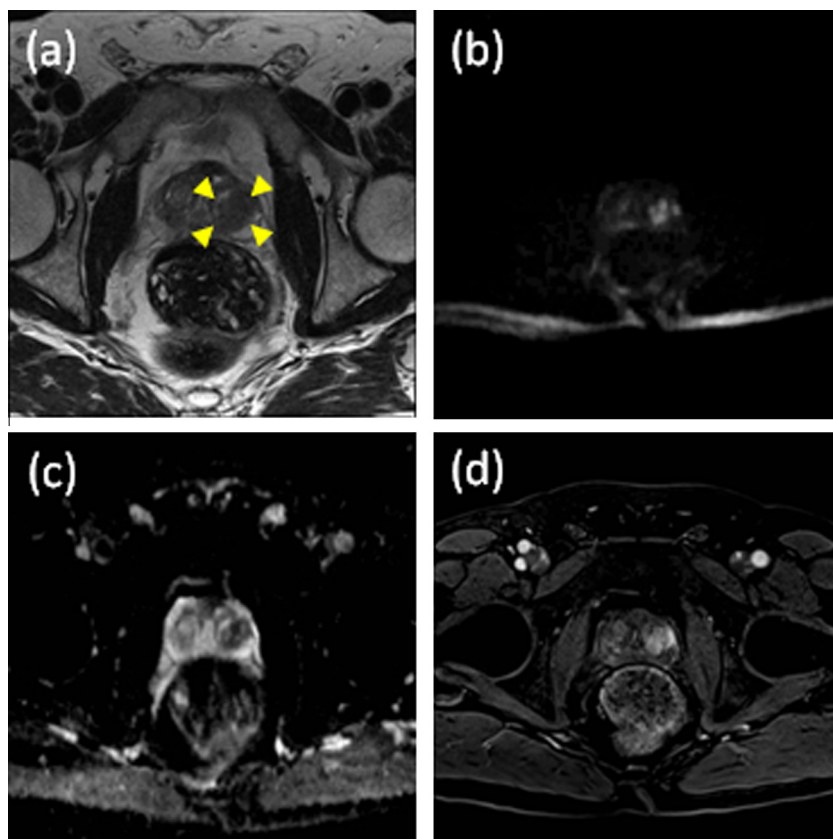
Fig. 2. Axial multi-parametric MR images from the prostate patient ((a) *T*2 weighted, (b) *b* = 1400 s/mm^2 DW image, (c) Apparent diffusion coefficient map, and (d) early post contrast *T*1 DCE). Yellow arrows indicate the area of peripheral zone prostate cancer. (For interpretation of the references to colour in this figure legend, the reader is referred to the web version of this article.)

For the undersampling pattern, phase encoding lines were randomly selected per volume and per time frame from a distribution where the centre of **k**-space was more densely sampled. Undersampling patterns for 4 and 8-fold acceleration were generated using a Monte-Carlo algorithm to generate a sampling pattern with minimum peak interference (Lustig et al., 2007).

3.3. Generation of prostate DCE (**k**, t)-data

The local institutional review board approved the study and waived the requirement for individual consent for the retrospective analysis of patient data collected as part of clinical trials/routine care (R&D No: 12/0195 date: 16/7/2012).

A prostate patient with significant peripheral zone prostate cancer (definition for clinically significant cancer was ⩾Gleason 3 + 4 or ⩾4 mm cancer core length) underwent prostatic multi-parametric MRI (*T*2, DCE and diffusion weighted MRI; Fig. 2) prior to template-prostate-mapping (TPM) biopsies as part of standard of care.

Imaging used a 1.5 T static magnet (Avanto, Siemens, Erlangen, Germany) and pelvic phased array coil. 0.2 mg/kg (maximum 20 mg) of spasmolytic (Bucsopan; Boehringer Ingelheim, Germany) was administered intravenously to reduce peristalsis. DCE-MRI was performed with a *T*1 weighted volumetric FLASH sequence with TR/TE 5.61/2.5 ms, flip angle 15°, field of view 269 mm, slice thickness 3 mm, temporal resolution of 16 s, and number of time points 35.

The original DCE images were then projected to (**k**, t)-space with fast Fourier transformation where normally distributed noise was added; undersampling masks for 4 and 8-fold acceleration were generated as described in Section 3.2. Noise was added directly to (**k**, t)-space MR data. Note that noise in the original magnitude MR images is considered as signal when used in simulations. Similar to the abdominal data, the level of applied noise was adjusted to match the noise level of prostate images.

3.4. Quantitative evaluation

The proposed direct method was compared with the Indirect(ZF-FFT) and the Indirect(ktFOCUSS) methods. All comparisons were conducted for fully sampled (FS), 4 and 8-fold undersampled (US4 and US8 respectively) (**k**, t)-data.

For the abdominal DCE phantom the kinetic maps from the different methods were compared using an entropy similarity metric (mutual information) to assess which method matches the ground truth kinetic parameters best. Similarly we examined which DCE images (reconstructed with ZF-FFT, kt-FOCUSS or estimated from the parameters w for the direct method) best matched the DCE images generated from the ground truth kinetic parameters.

For the prostate data where no ground truth kinetic maps were available, an experienced radiologist assessed the derived kinetic maps to examine which method depicts cancer best.

4. Results

4.1. Abdominal simulated DCE phantom

Kinetic maps of v_p, K_{trans}, v_e are shown in Figs. 3–5. Fig. 3 shows the ground truth kinetic parameters and the ones derived from the Indirect(FFT) and the direct method for fully sampled data. Figs. 4 and 5 show kinetic parameters of the Indirect(ZF-FFT), Indirect(ktFOCUSS) and the direct method derived from 4 and 8-fold undersampled data. Figs. 3–5 illustrate better correspondence of
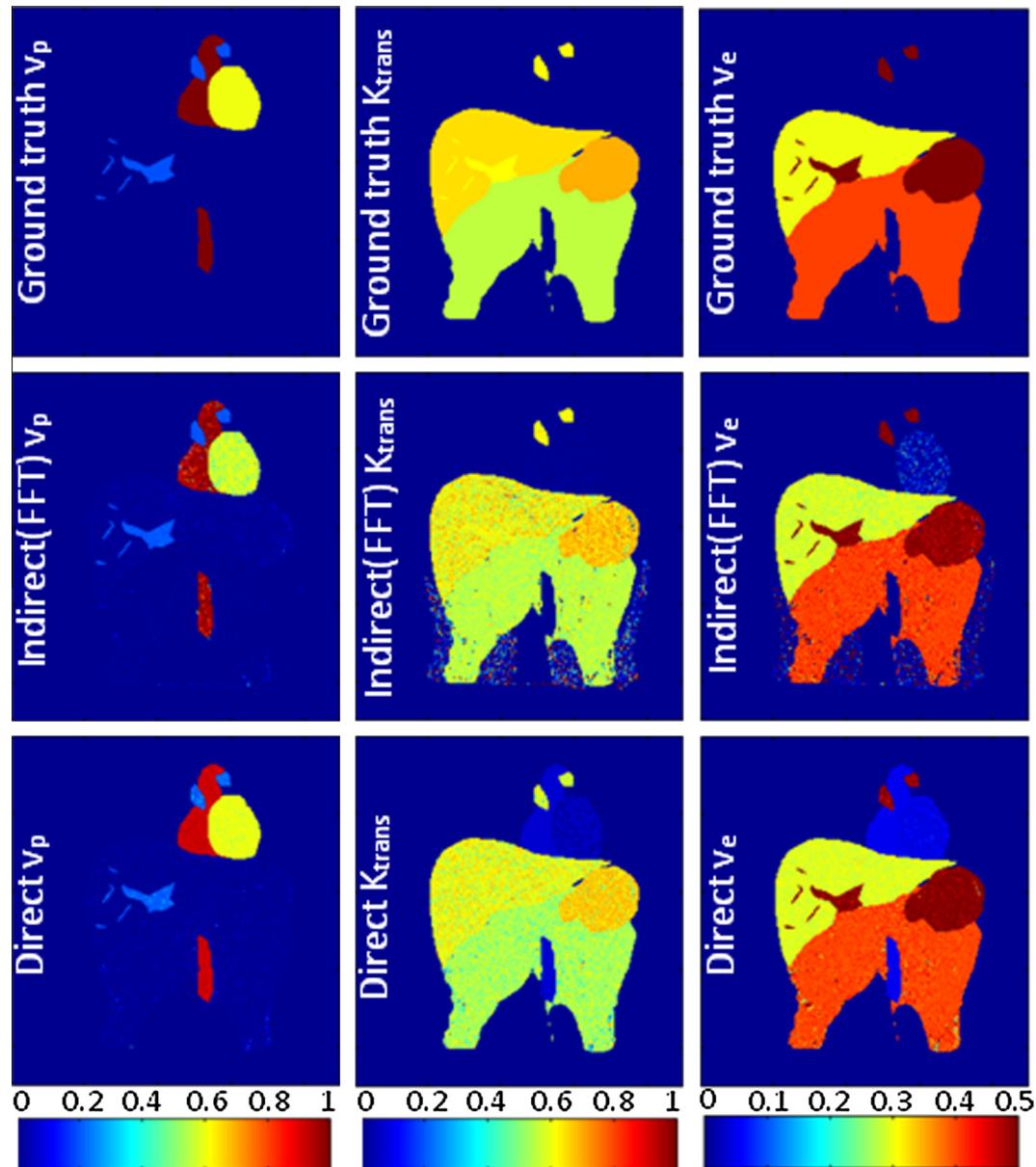
Fig. 3. Top row illustrates ground truth kinetic maps v_p, K_{trans}, v_e used to generate the abdominal simulated DCE phantom. Second and third rows show the kinetic maps v_p, K_{trans}, v_e derived from the Indirect(FFT) and **direct** methods for fully sampled (k, t)-data.

the direct kinetic parameters with the ground truth kinetic parameters than the other two methods. This was verified quantitatively as shown in Table 1. Direct kinetic parameters yield consistently higher mutual information (similarity with the ground truth kinetic parameters) than the Indirect(ZF-FFT) or Indirect (ktFOCUSS) kinetic parameters.

Fig. 6 illustrates reconstructed DCE images with ZF-FFT, kt-FOCUSS and the direct method. For the direct method DCE images are calculated indirectly via the kinetic parameters. Table 2 shows that direct method provided a better match (higher mutual information) to the ground truth DCE images than kt-FOCUSS reconstructed DCE images.

To examine how reproducible the results of the direct method are, we ran the direct method for 8-fold undersampled abdominal DCE ($\mathbf{k}$, t)-space data for 10 different initialization combinations where initial values of the kinetic parameters ranged from 0 to 0.3 for v_p, from 0.24 to 0.8 for K_{trans} and from 0.2 to 0.8 for v_e. To examine how much the results varied given different initializations, we

calculated the relative standard deviation $rstd_y$ of the residual $\|y(\mathbf{k}, t) - S(\mathbf{k}, t)\|_2^2$ and, the median of relative standard deviations median($rstd_{vp}$), median($rstd_{Ktrans}$) and median($rstd_{ve}$) across each kinetic map separately. The calculated relative standard deviations were $rstd_y = 0.8\%$, median($rstd_{vp}$) = 7%, median($rstd_{Ktrans}$) = 5%, median($rstd_{ve}$) = 4%.

4.1.1. Motion incorporation

To illustrate how the current algorithm (and the Indirect(ktFOCUSS) approach) would be affected by respiratory motion, we regenerated the abdominal DCE phantom including motion derived from non-rigid registration (Rueckert et al., 1999) of the free breathing $T1$ weighted time series. The range of motion was [2.87 2.63] pixels × 1.95 mm in the right–left and [8.35 1.81] pixels × 1.95 mm in the superior inferior directions. Since an image registration step could be easily incorporated prior to DCE analysis, DCE images reconstructed with kt-FOCUSS were registered using RDDR algorithm (Hamy et al., 2014) which was
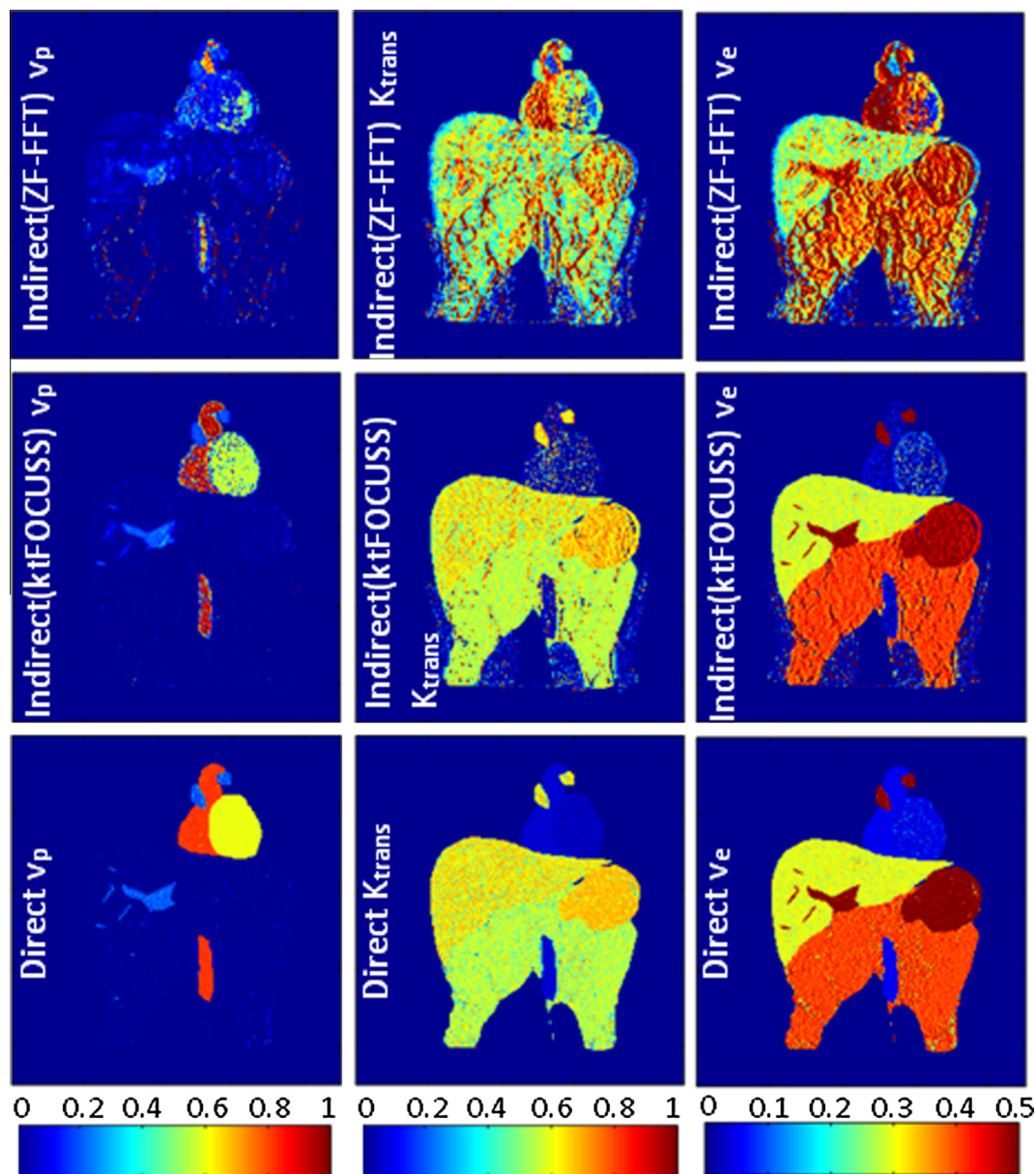
Fig. 4. Kinetic maps v_p, K_{trans}, v_e derived from the Indirect(ZF-FFT), Indirect(ktFOCUSS) and direct methods for 4-fold undersampled (US4) data of the abdominal simulated DCE phantom.

developed specifically for DCE registration. Fig. 7 illustrates the kinetic maps of the direct and the Indirect(ktFOCUSS) method with and without the registration step for 8-fold undersampling. All the kinetic maps have degraded due to motion (compare to Figs. 3 and 5) but direct kinetic maps exhibit some resilience to motion.

4.2. Prostate data

Kinetic maps of K_{trans} are illustrated in Fig. 8, where the Indirect(ZF-FFT), Indirect(ktFOCUSS) and the direct methods are compared for fully sampled, 4 and 8-fold undersampled ($\mathbf{k}$, t)-space data. Dikaios et al. (2013b) showed that K_{trans} is better at classifying peripheral zone prostate cancer compared to v_p and v_e; hence this was selected for illustration. Kinetic maps from the direct reconstruction depict the peripheral zone prostate cancer better than the Indirect(ZF-FFT) and Indirect(ktFOCUSS) methods.

DCE images calculated from the direct kinetic parameters were compared with DCE images reconstructed with ZF-FFT and kt-FOCUSS (Fig. 9). Direct DCE images have good contrast between different features, and resemble the original DCE image shown in Fig. 2(d) even for high undersampling factors. Although not easily visible direct DCE images in Fig. 9 are contaminated by high frequency noise.

5. Discussion

5.1. Functional imaging

Functional parameters related to the pathophysiology (e.g. perfusion, vessel permeability, metabolism) or the tissue (e.g. diffusion, $T1$ and $T2$ relaxation times) are classifiers of diseases. Parametric maps are usually estimated indirectly via images.

In this work we derived the parametric maps directly from the measurements (i.e. from ($\mathbf{k}$, t)-space for DCE MRI). Direct parametric reconstruction has been applied in dynamic PET (Tsoumpas et al., 2008) and demonstrated better recovery of the associated parameters.
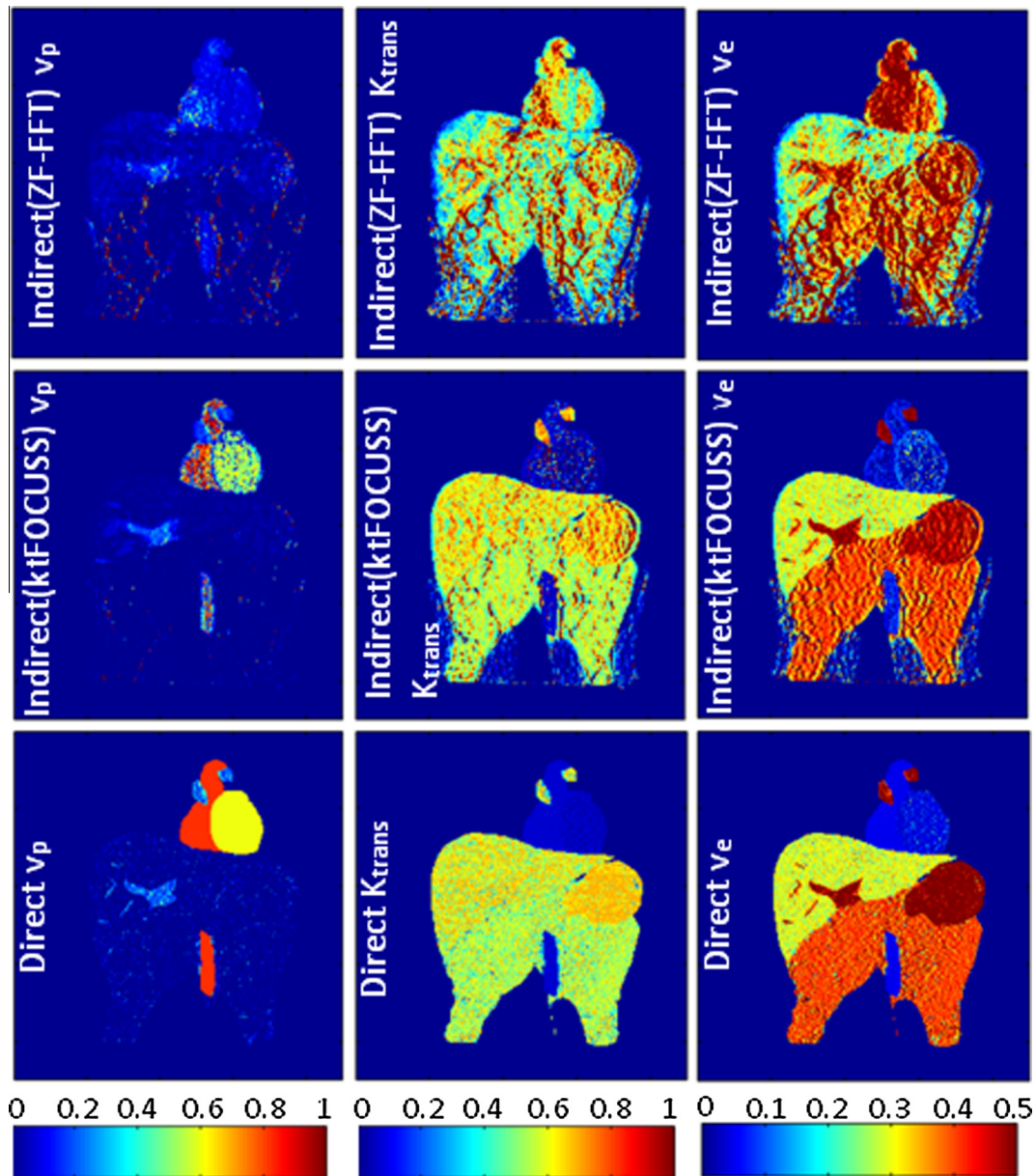
Fig. 5. Kinetic maps v_p, K_{trans}, v_e derived from the Indirect(ZF-FFT), Indirect(ktFOCUSS) and direct methods for 8-fold undersampled (US8) data of the abdominal simulated DCE phantom. The display range of v_p, K_{trans} was [0 (blue), 1 (red)] and of v_e was [0 (blue), 0.5 (red)]. (For interpretation of the references to colour in this figure legend, the reader is referred to the web version of this article.)

A Bayesian inference algorithm is suggested to perform direct parametric reconstruction from highly undersampled DCE-MRI measurements. The proposed algorithm (denoted as direct) is based on a complete noise model of the measured data, and employs a low-rank prior to ensure local coherence in time.

5.2. Summary of results

Direct kinetic maps of the abdominal DCE phantom accurately recovered the ground truth kinetic parameters even for highly undersampled (**k**, t)-space data (up to 8-fold), outperforming indirect schemes (using ZF-FFT and kt-FOCUSS reconstruction). Abdominal DCE images estimated from direct kinetic maps were also more accurate than abdominal DCE images reconstructed with ZF-FFT or kt-FOCUSS. The bias of the direct method varies across different organs (Fig. 3), this is clearly visible in areas with different kinetics (i.e. heart, aorta) where the bias is approximately 10 times

higher than the rest of the organs. This has also been observed in PET direct reconstruction (Tsoumpas et al., 2008; Rahmim et al., 2012), where the strong correlation between the two temporal basis functions of the Patlak plot slows down the convergence. To overcome this problem, PET direct algorithms that decouple this temporal correlation were suggested (Rahmim et al., 2012), similar ideas could be investigated for the proposed direct algorithm.

Direct kinetic maps of the prostate (i.e. K_{trans}) depict peripheral zone cancer better than indirect schemes with a clearer benefit at higher undersampling factors. The differences between the direct and the indirect schemes can be identified as follows:

i. Indirect schemes (using either FFT or ktFOCUSS reconstruction) employ non-linear fitting (i.e. simplex algorithm) to derive the kinetic maps. Non-linear fitting is prone to hit local minima in the presence of noise (and aliasing artefacts related to undersampling).

Table 1
Similarity measurements (based on mutual information) between ground truth kinetic parameters and kinetic parameters derived from the indirect methods using ZF-FFT or kt-FOCUSS and the direct method for the abdominal simulated DCE phantom. Results are shown for fully sampled data (FS) and for undersampling factors 4 (US4) and 8 (US8). Correspondence is best when mutual information is increased.

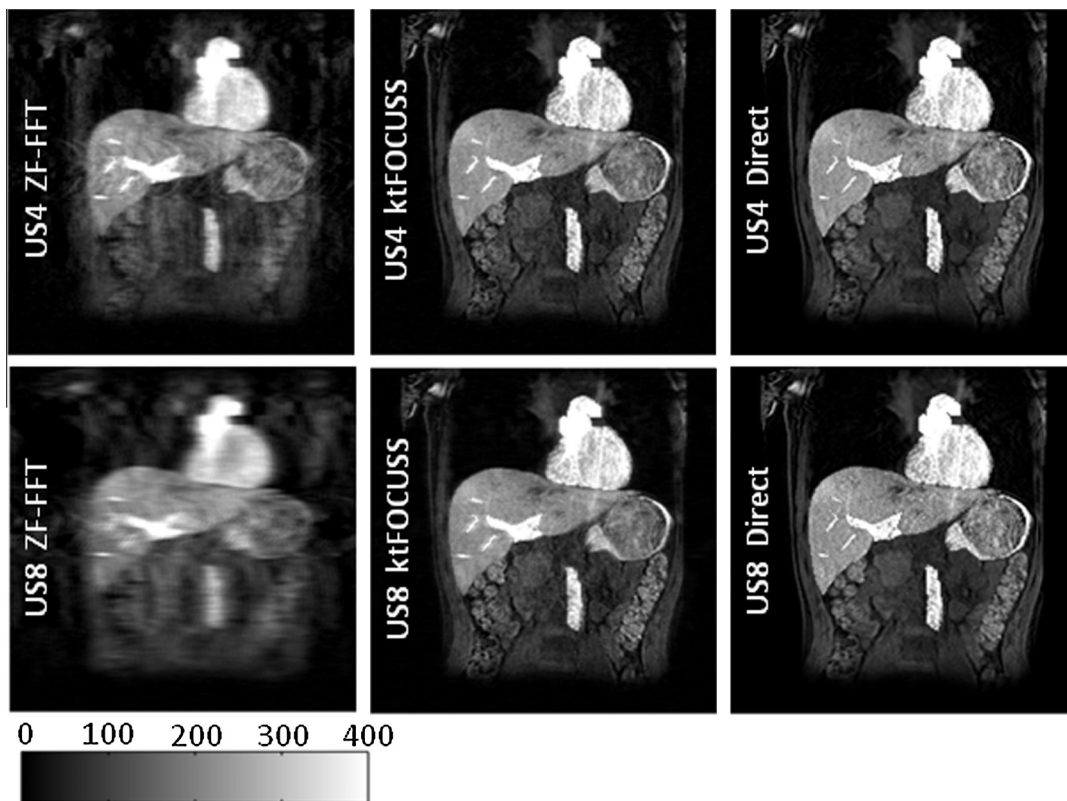|		v_p	K_{trans}	v_e	t_0
FS	Indirect(FFT)	0.433	0.597	1.194	1.330
	Direct	0.441	0.632	1.236	1.411
US4	Indirect(ZF-FFT)	0.267	0.383	0.693	1.202
	Indirect(ktFOCUSS)	0.379	0.550	1.105	1.305
	Direct	0.429	0.603	1.120	1.368
US8	Indirect(ZF-FFT)	0.246	0.351	0.636	1.179
	Indirect(ktFOCUSS)	0.344	0.540	0.944	1.251
	Direct	0.416	0.585	1.118	1.307

Fig. 6. Reconstructed DCE images of the abdominal simulated DCE phantom using ZF-FFT, kt-FOCUSS and the direct method for 4-fold (US4) and 8-fold (US8) undersampling.

Table 2
Similarity measurements (based on mutual information) between ground truth dynamic contrast enhancement images (DCE) and DCE images reconstructed with ZF-FFT, kt-FOCUSS and the Direct method (where the DCE images are estimated indirectly from the kinetic parameters) for the abdominal simulated DCE phantom. Results are shown for fully sampled data (FS) and for undersampling factors 4 (US4) and 8 (US8). Correspondence is best when mutual information is increased.

		Reconstructed DCE images
FS	Indirect(FFT)	3.370
	Direct	4.430
US4	Indirect(ZF-FFT)	2.185
	Indirect(ktFOCUSS)	3.204
	Direct	4.215
US8	Indirect(ZF-FFT)	1.933
	Indirect(ktFOCUSS)	2.760
	Direct	3.865

ii. The direct method allows for a complete modelling of the noise (of the acquired data) in the parameter estimation process.
iii. The direct method has been implemented in a Bayesian inference framework (using MCMC), which has a theoretic guarantee to converge if run long enough (Gelman and Shirley, 2011).

5.3. Methodological limitations

One of the limitations of the suggested direct algorithm is that it does not explicitly account for patient motion, and may thus be more suitable for organs such as the prostate, where motion is of low magnitude. Results (Fig. 7) indicate that whilst indirect methods can incorporate a registration step, the direct approach has an inherent robustness to motion.
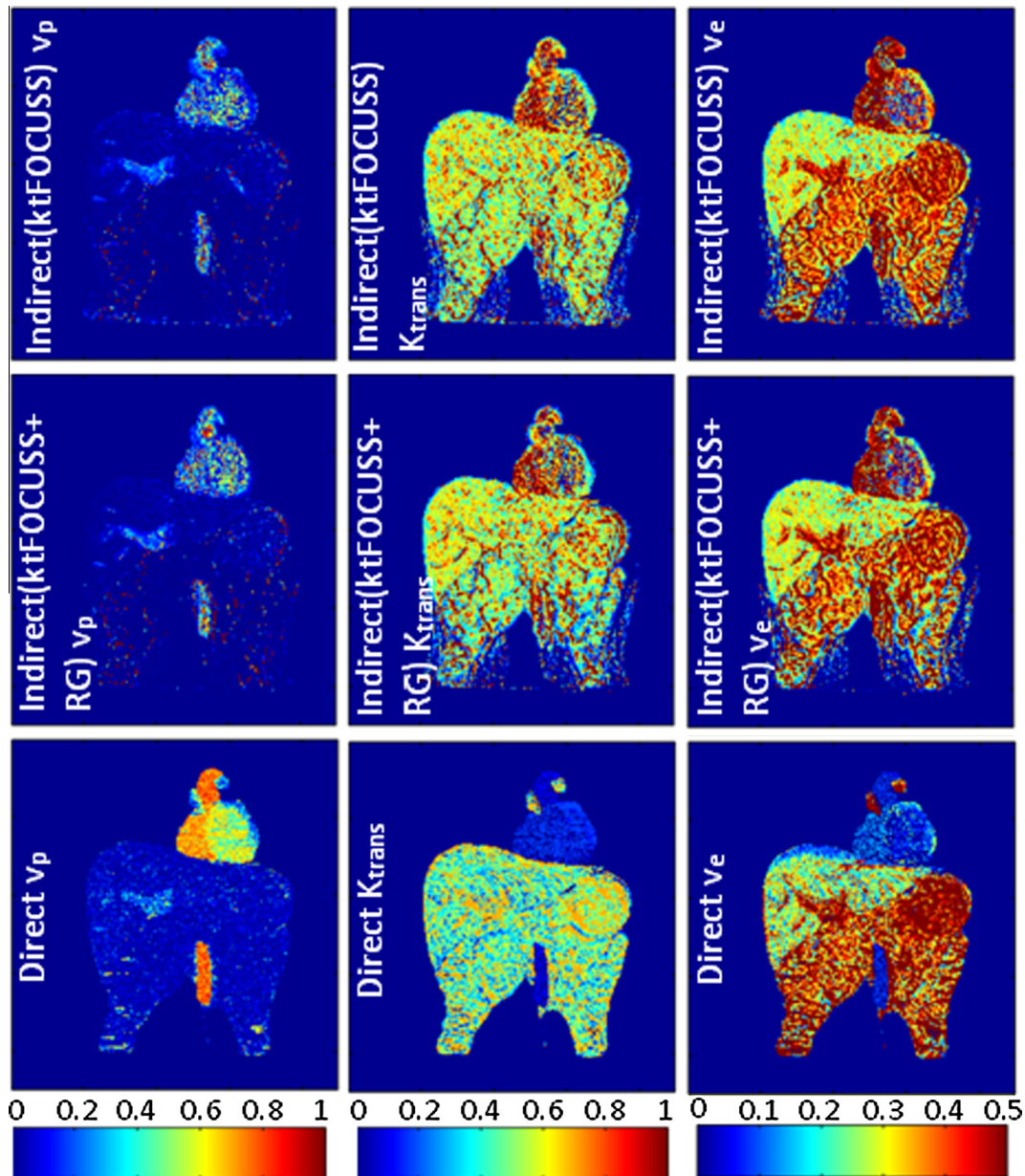
Fig. 7. Kinetic maps v_p, K_{trans}, v_e derived from simulations of 8-fold undersampled data reconstructed with Indirect(ktFOCUSS) – no registration, Indirect(ktFOCUSS + RG) – using RDDR registration, and. the direct method with no explicit motion correction.

If the motion field during the acquisition is known, it could be easily incorporated into the direct method by modelling the enhancement signal accordingly

$$x'(\mathbf{r}, t; w) = D^{s \rightarrow t} x(\mathbf{r}, t; w)$$

$D^{s \rightarrow t}$ is a motion matrix that warps the pixels from motion state s (reference image) to the motion state at time t.

Rigid motion can be estimated with optical tracking devices but estimating non-rigid motion in advance is less trivial. There is ongoing work using motion models (e.g. King et al., 2012) that could be applicable in DCE imaging. Alternatively, motion fields could be estimated in a joint reconstruction scheme during the minimization process, where besides the kinetic parameters, the motion field will also be updated (Jacobson and Fessler, 2003; Odille et al., 2008) where he proposed a joint reconstruction scheme for motion correction in PET.

The current implementation assumes that the pharmacokinetics are described by the extended Tofts model. The forward signal model in the direct approach should reflect signal changes throughout the entire field of view and the Tofts model with a single bolus input may not be adequate in the liver, where a dual input signal compartment model is preferred (Materne et al., 2000). The effect of having organs with enhancement that is not adequately described by the kinetic model used has been discussed by Kotasidis et al. (2011). To apply the direct approach on clinical abdominal DCE MRI, the algorithm could be modified to identify organs where the Tofts model is inadequate and apply the correct pharmacokinetic model. Indirect approaches process image pixels independently and an incorrect model would affect only the image regions where the model is not applicable.

The direct method is more computationally expensive than the indirect methods (depending on the number of iterations). For the current settings it can be up to 7 times slower. The computational
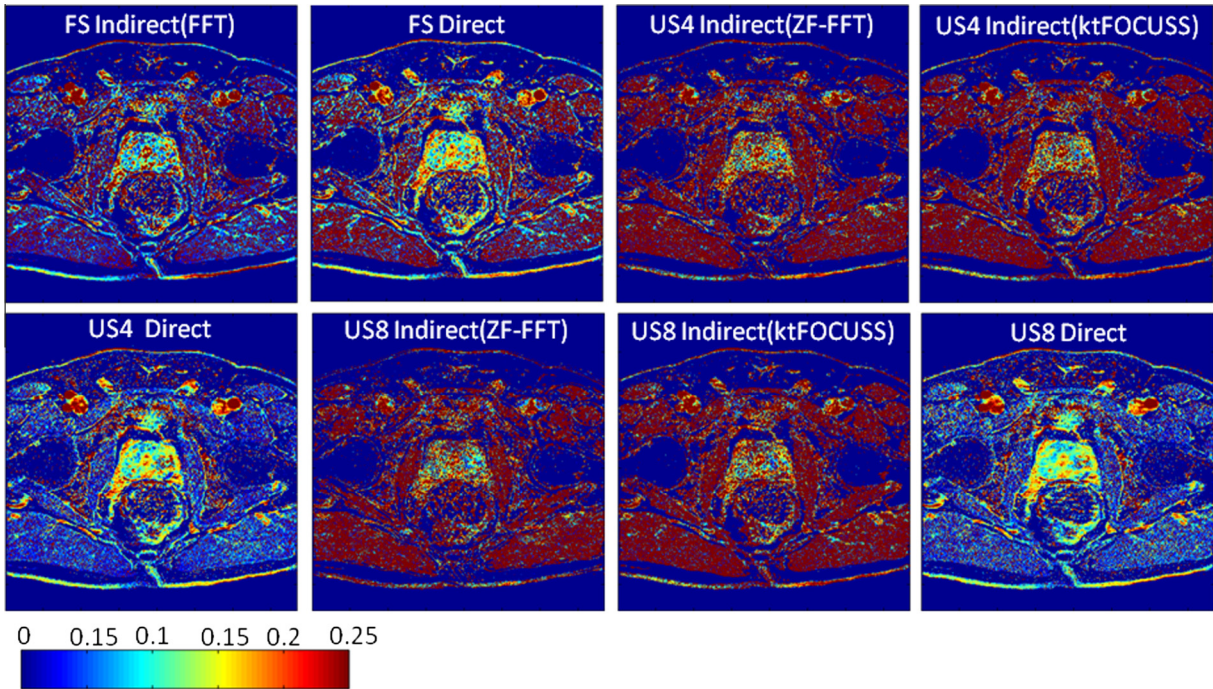
Fig. 8. Kinetic maps K_{trans} of the prostate data derived from the Indirect(ZF-FFT), Indirect(ktFOCUSS), and the direct methods for fully sampled (FS), 4-fold (US4) and 8-fold (US8) undersampled data.
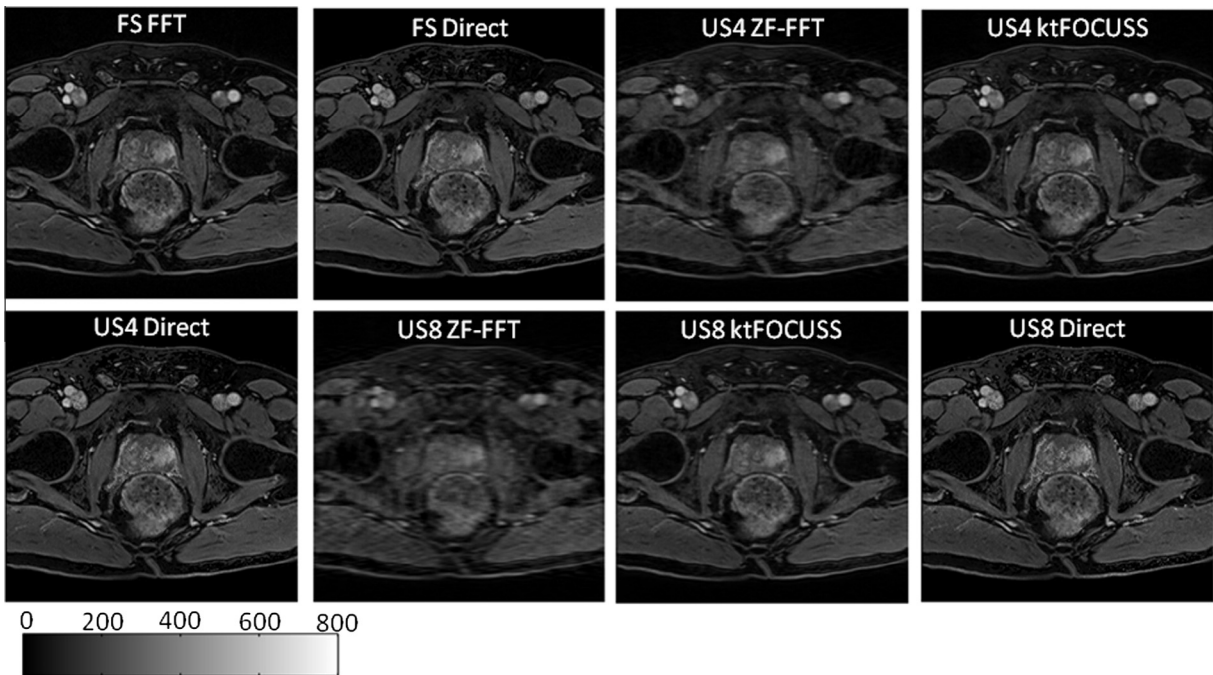

Fig. 9. Reconstructed DCE images of the prostate data using ZF-FFT, kt-FOCUSS and the direct method for fully sampled (FS), 4-fold (US4) and 8-fold (US8) undersampling.

cost of the direct method will depend of course on the number of tuning iterations, but with the aforementioned settings (using Matlab 7.12.0 on a Xeon 1.6 GHz with 12 GB RAM) results were achieved in approximately 17 h.

5.4. Clinical implications

Pharmacokinetic parameters related to the enhancement have been advocated as a biomarker of cancer. For prostate cancer local-ization DCE-MRI remains the mainstay of commercial computer aided diagnostic software (Engelbrecht et al., 2003, Puech et al., 2004). Dikaios et al. (2013a,b) proposed the following logistic regression diagnostic model for peripheral zone prostate cancer based on an early enhancement image (E_{early}) and a K_{trans} map that predicts cancer with a receiver operator characteristic (ROC) area under curve (AUC) of 0.754 (following leave-one-out analysis)

$$P_{PZ} = \frac{e^{-5.83+1.29 \cdot K_{trans}+3.2 \cdot E_{early}}}{e^{-5.83+1.29 \cdot K_{trans}+3.2 \cdot E_{early}} + 1} \tag{19}$$
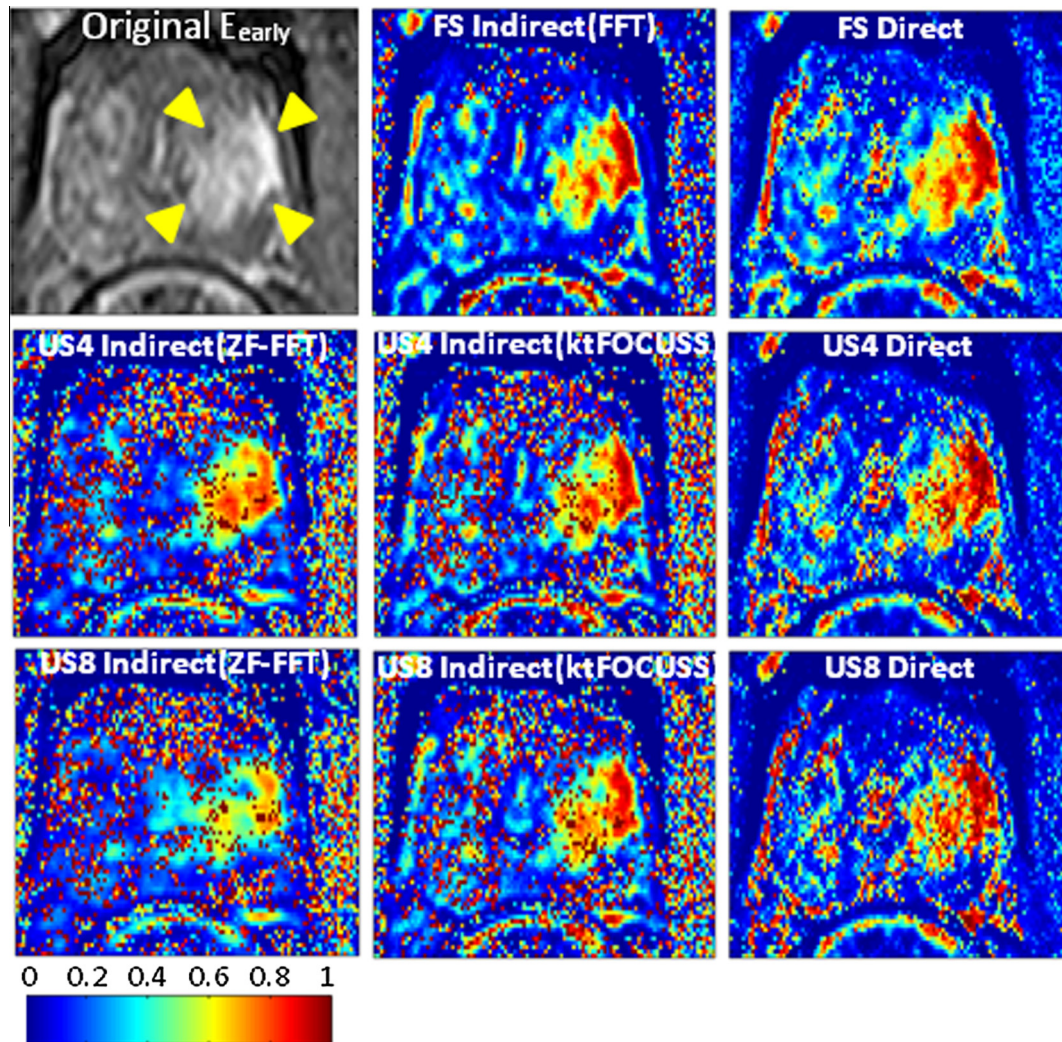
Fig. 10. Prostate cancer predictive probability maps estimated from kinetic parameters (E_{early}, K_{trans}) derived from the (ZF-FFT), Indirect(ktFOCUSS), and the direct methods for fully sampled (FS-1st row), 4-fold (US4-2nd row) and 8-fold (US8-3rd row) undersampling. An early enhancement DCE E_{early} image that depicts the area of the cancer (yellow arrows) is shown. (For interpretation of the references to colour in this figure legend, the reader is referred to the web version of this article.)

where P_{PZ} is the predictive probability. Fig. 10 illustrates predictive probability maps calculated from an E_{early} image and a K_{trans} map derived from the direct and indirect methods. An experienced radiologist reviewed the probability maps (after reviewing the multiparametric MRI images (i.e. $T2$ weighted, apparent diffusion coefficient, $b = 1400\,s/mm^2$ diffusion weighted, and an early enhancement image)). The probabilities within the tumour for the direct parameters are higher than the ones for indirect methods. In addition the morphology of the tumour is retained within the probability map of the direct kinetic parameters, even for 8-fold undersampling of the ($\mathbf{k}$, t)-space data.

6. Conclusion

The concept of direct parametric reconstruction from ($\mathbf{k}$, t)-space data is a promising challenge as it extracts the functional information which dictates the signal alterations directly from the measurements. This paper provides a Bayesian inference framework to accurately estimate pharmacokinetic parameters from undersampled ($\mathbf{k}$, t)-space data. Results on a simulated abdominal DCE phantom and prostate data indicate that the proposed scheme recovers accurate parametric kinetic maps, and in

an example prostate cancer case, represents better the tumour morphology, even for highly undersampled measurements.

References

Agrawal, S. et al., 2012. An exploratory study into the role of dynamic contrast-enhanced (DCE) MRI metrics as predictors of response in head and neck cancers. Clin. Radiol. 67 (9), 1–5.

Andersen, E.K. et al., 2013. Pharmacokinetic parameters derived from dynamic contrast enhanced MRI of cervical cancers predict chemoradiotherapy outcome. Radiother. Oncol. 107 (1), 117–122.

Armbruster, M. et al., 2014. Evaluation of Neuroendocrine liver metastases: a comparison of dynamic contrast-enhanced magnetic resonance imaging and positron emission tomography/computed tomography. Invest. Radiol. 49 (1), 7–14.

Banerji, A. et al., 2012. DCE-MRI model selection for investigating disruption of microvascular function in livers with metastatic disease. J. Magn. Reson. Imaging 35 (1), 196–203.

Buckley, D.L. et al., 2004. Prostate cancer: evaluation of vascular characteristics with dynamic contrast-enhanced T1-weighted MR imaging-initial experience. Radiology 233 (3), 709–715.

Cai, J.F., Candes, E.J., Shen, Z., 2008. A singular value thresholding algorithm for matrix completion. SIAM J. Optim. 20, 1956–1982.

Combettes, P.L., Wajs, V.R., 2005. Signal recovery by proximal forward-backward splitting. Multiscale Model. Simul. 4, 1168–1200.

Coupe, P. et al., 2010. Robust Rician noise estimation for MR images. Med. Image Anal. 14, 483–493.

Dikaios, N., 2013a. Noise estimation from averaged diffusion weighted images: can unbiased quantitative decay parameters assist cancer evaluation? Magn. Reson. Med. (ahead of print).

Dikaios, N. et al., 2013b. Derivation and comparison of site specific peripheral and transition zone quantitative DCE MRI logistic regression models for prostate cancer detection: does cancer location matter? Proc. Int. Soc. Magn. Reson. Med. 21, 577.

Donoho, D.L., 2006. Compressed sensing. IEEE Trans. Inf. Theory 52, 1289–1306.

Engelbrecht, M.R. et al., 2003. Discrimination of prostate cancer from normal peripheral zone and central gland tissue by using dynamic contrast-enhanced MR imaging. Radiology 229 (1), 248–254.

Furman-Haran, E. et al., 2013. Standardization of Radiological Evaluation of Dynamic Contrast Enhanced MRI: Application in Breast Cancer Diagnosis. Technology Cancer Research Treatment (ahead of print).

Gao, H. et al., 2011. Robust principal component analysis-based four-dimensional computed tomography. Phys. Med. Biol. 56, 3181–3198.

Gelman, A., Shirley, K., 2011. Inference from simulations and monitoring convergence. In: Brooks, S., Gelman, A., Jones, G., Meng, X.L. (Eds.), Handbook of Markov Chain Monte Carlo. CRC Press.

Gorodnitsky, I.F., George, J.S., Rao, B.D., 1995. Neuromagnetic source imaging with FOCUSS: a recursive weighted minimum norm algorithm. Electroencephalogr. Clin. Neurophysiol. 95, 231–251.

Griswold, M.A. et al., 2002. Generalized autocalibrating partially parallel acquisitions (GRAPPA). Magn. Reson. Med. 47, 1202–1210.

Gudbjartsson, H., Patz, S., 2005. The Rician distribution of noisy MRI data. Magn. Reson. Med., 910–914.

Hamy, V. et al., 2014. Respiratory motion correction in dynamic MRI using robust data decomposition registration – application to DCE-MRI. Med. Image Anal. 18, 301–313.

Jacobson, M.W., Fessler, J.A., 2003. Joint estimation of image and deformation parameters in motion-corrected PET. In: IEEE Nuclear Science Symposium Conference, Record, = 5, pp. 3290–3294.

Jain, R., 2013. Measurements of tumor vascular leakiness using DCE in brain tumors: clinical applications. NMR Biomed. 26, 1042–1049.

Jung, H., Ye, J.C., Kim, E.Y., 2007. Improved *k–t* BLAST and *k–t* SENSE using FOCUSS. Phys. Med. Biol. 52, 3201–3226.

King, A.P. et al., 2012. Thoracic respiratory motion estimation from MRI using a statistical model and a 2-D image navigator. Med. Image Anal. 16 (1), 252–264.

Kotasidis, F.A., et al., 2011. Impact of erroneous kinetic model formulation in direct 4D image reconstruction. In: IEEE Nuclear Science Symposium and Medical Imaging Conference Record, pp. 2366–2367.

Lingala, S.G. et al., 2011. Accelerated dynamic MRI exploiting sparsity and low-rank structure: *k–t* SLR. IEEE Trans. Med. Imaging 30, 1042–1054.

Lustig, M., Donoho, D., Pauly, J.M., 2007. Sparse MRI: the application of compressed sensing for rapid MR imaging. Magn. Resonan. Med. 58, 1182–1195.

Materne, R. et al., 2000. Non-invasive quantification of liver perfusion with dynamic computed tomography and a dual-input one-compartmental model. Clin. Sci. (Lond.) 99, 517–525.

Melbourne, A., Atkinson, D., Hawkes, D., 2008. Influence of organ motion and contrast enhancement on image registration. Med. Image Comput. Comput. – Assist. Interven. 11, 948–955.

Odille, F. et al., 2008. Generalized MRI reconstruction including elastic physiological motion and coil sensitivity encoding. Magn. Reson. Med. 59, 1401–1411.

Parker, G.J. et al., 2006. Experimentally-derived functional form for a population-averaged high-temporal-resolution arterial input function for dynamic contrast-enhanced MRI. Magn. Reson. Med. 56, 993–1000.

Press, W.H. et al., 1984. Numerical Recipes in C, Cambridge, New York.

Pruessmann, K.P. et al., 1999. SENSE: sensitivity encoding for fast MRI. Magn. Reson. Med. 42, 952–962.

Puech, P. et al., 2004. Computer-assisted diagnosis of prostate cancer using DCE-MRI data: design, implementation and preliminary results. Int. J. Comput. Assist. Radiol. Surg. 4 (1), 1–10.

Rahmim, A. et al., 2012. Direct 4D parametric imaging for linearized models of reversibly binding PET tracers using generalized AB-EM reconstruction. Phys. Med. Biol. 57 (3), 733–755.

Rosenthal, J.S., 2010. Optimal proposal distributions and adaptive MCMC. In: Brooks, S., Gelman, A., Jones, G., Meng, X.-L. (Eds.), Chapter for MCMC Handbook.

Rueckert, D. et al., 1999. Nonrigid registration using free-form deformations: application to breast MR images. IEEE Trans. Med. Imaging 18, 712–721.

Tofts, P.S., 1997. Modeling tracer kinetics in dynamic Gd-DTPA MR imaging. J. Magn. Reson. Imaging 7, 91–101.

Tofts, P.S., 2010. T1-Weighted DCE Imaging Concepts: Modelling, Acquisition and Analysis, pp. 1–5.

Tsao, J., Kozerke, S., 2012. MRI temporal acceleration techniques. J. Magn. Reson. Imaging 36, 543–560.

Tsoumpas, C., Turkheimer, F.E., Thielemans, K., 2008. Study of direct and indirect parametric estimation methods of linear models in dynamic positron emission tomography. Med. Phys. 35, 1299–1309.